# CHEMICAL PHYSICS

# Protecting hot carriers by tuning hybrid perovskite structures with alkali cations

Ti Wang<sup>1,2</sup>, Linrui Jin<sup>1</sup>, Juanita Hidalgo<sup>3</sup>, Weibin Chu<sup>4</sup>, Jordan M. Snaider<sup>1</sup>, Shibin Deng<sup>1</sup>, Tong Zhu<sup>1,5</sup>, Barry Lai<sup>6</sup>, Oleg Prezhdo<sup>4</sup>, Juan-Pablo Correa-Baena<sup>3</sup>, Libai Huang<sup>1</sup>\*

Successful implementation of hot carrier solar cells requires preserving high carrier temperature as carriers migrate through the active layer. Here, we demonstrated that addition of alkali cations in hybrid organic-inorganic lead halide perovskites led to substantially elevated carrier temperature, reduced threshold for phonon bottleneck, and enhanced hot carrier transport. The synergetic effects from the Rb, Cs, and K cations result in ~900 K increase in the effective carrier temperature at a carrier density around 10<sup>18</sup> cm<sup>-3</sup> with an excitation 1.45 eV above the bandgap. In the doped thin films, the protected hot carriers migrate 100 s of nanometers longer than the undoped sample as imaged by ultrafast microscopy. We attributed these improvements to the relaxation of lattice strain and passivation of halide vacancies by alkali cations based on x-ray structural characterizations and first principles calculations.

Copyright © 2020 The Authors, some rights reserved; exclusive licensee American Association for the Advancement of Science. No claim to original U.S. Government Works. Distributed under a Creative Commons Attribution NonCommercial License 4.0 (CC BY-NC).

# INTRODUCTION

The theoretical maximum power conversion efficiency (PCE) of a hot carrier solar cell can be as high as 66% (1), substantially above the Shockley-Queisser limit (2). However, the efforts to apply the hot carrier strategy in practice have so far been hindered by hot carrier cooling that is usually much faster than the time needed to transport the charge carriers in conventional semiconductors (3). Hybrid organic-inorganic metal halide perovskite semiconductors have emerged as an exciting class of materials for high-performance solar cells with PCE over 24% (4-6). Recent studies revealed unusually slow picosecond carrier cooling coupled with long-range hot carrier transport, suggesting large potential of hot carrier solar cells based on hybrid perovskites (7, 8). At high carrier densities, the hot phonon bottleneck, further extends carrier cooling time scale up to hundreds of picoseconds (9-13). Hot carrier cooling and transport in hybrid perovskites have been shown to differ from traditional semiconductors substantially due to the interplay between large polaron formation and a dynamic ionic lattice (7, 14, 15).

Despite the impressive progress, challenges remain in achieving high carrier temperature at reasonable carrier density while maintaining thermal stability. Taking advantage of the programmable and flexible structure of hybrid perovskites, a possible route to address these challenges is through fine-tuning of the structure to influence phonon and defect scattering processes (16, 17) and achieve better stability. The general structure for hybrid perovskites is ABX<sub>3</sub>; the B site is a divalent metallic atom (typically Pb<sup>2+</sup> or Sn<sup>2+</sup>), the X site is a halide (Cl, Br, and I), and the A site is an intercalating cation. The A site cation can be either organic, such as CH<sub>3</sub>NH<sub>3</sub>+ (methylammonium, MA<sup>+</sup>) and CH(NH<sub>2</sub>)<sub>2</sub>+ (formamidinium, FA<sup>+</sup>), or inorganic, for instance, Cs<sup>+</sup>. Success has been achieved recently with the incorporation

of a small amount of alkali metals (such as  $Rb^+$  and  $K^+$ ), demonstrating stabilized perovskite structures at high temperatures and suppression of ion migration (6, 18, 19). The addition of alkali cations has also been shown to reduce the recombination of cooled carriers at the band edge by passivating defects (20–23); however, the influence of the alkali cations on the dynamics of hot carriers above the band edge is unknown.

Here, we showed that the incorporation of alkali cations can markedly modify hot carrier relaxation and transport by using ultrafast transient absorption (TA) spectroscopy and microscopy combined with first principles calculations. The synergetic effects from the Rb, Cs, and K cations lead to properties beneficial for hot carrier solar cells, including elevated carrier temperature over tens of picosecond time scale and enhanced hot carrier transport over hundreds of nanometer length scale. By suppressing the loss of excessive energy to defects, the alkali cations also reduce the threshold carrier density for achieving picosecond carrier cooling via hot phonon effect by an order of magnitude. These results underscore the opportunities in designing optimal hybrid perovskite structures for hot carrier solar cells.

# **RESULTS**

# Sample characterizations

To explore composition tuning to influence hot carrier cooling and transport, we used (MAPbBr<sub>3</sub>)<sub>0.17</sub>(FAPbI<sub>3</sub>)<sub>0.83</sub> that was commonly used in high-performance solar cells as the reference sample and that is referred to as "MAFA" throughout the article (6). Five different cation combinations were investigated in this work. Three triple cation perovskites were made by adding either 5% of cesium iodide (CsI), or 5% of rubidium iodide (RbI), or 5% of potassium iodide (KI) to the MAFA reference, named "CsMAFA," "RbMAFA," and "KMAFA," respectively. The percentage corresponds to the molar concentration of the alkali cations in the perovskite precursor solution. The quadruple cation perovskite material containing both 5% of Cs and 5% of Rb is referred to as RbCsMAFA. Last, a quintuple cation composition with 5% Cs, 5% Rb, and 5% K is called RbCsKMAFA. Polycrystalline thin films with thickness of 400 to 450 nm were deposited on 0.17-mmthick glass coverslips (a scanning electron microscopy image is shown in fig. S1A).

<sup>&</sup>lt;sup>1</sup>Department of Chemistry, Purdue University, West Lafayette, IN 47907, USA. <sup>2</sup>School of Physics and Technology, Center for Nanoscience and Nanotechnology, and Key Laboratory of Artificial Micro- and Nano-structures of Ministry of Education, Wuhan University, Wuhan 430072, China. <sup>3</sup>School of Materials Science and Engineering, Georgia Institute of Technology, Atlanta, GA 30332, USA. <sup>4</sup>Departments of Chemistry and Physics and Astronomy, University of Southern California, Los Angeles, CA 90007, USA. <sup>5</sup>Laser Micro/Nano Fabrication Laboratory, School of Mechanical Engineering, Beijing Institute of Technology, No. 5 Zhongguancun South Street, Beijing 100081, China. <sup>6</sup>Advanced Photon Source, Argonne National Laboratory, 9700 Cass Ave., Lemont, IL 60439, USA.

<sup>\*</sup>Corresponding author. Email: libai-huang@purdue.edu

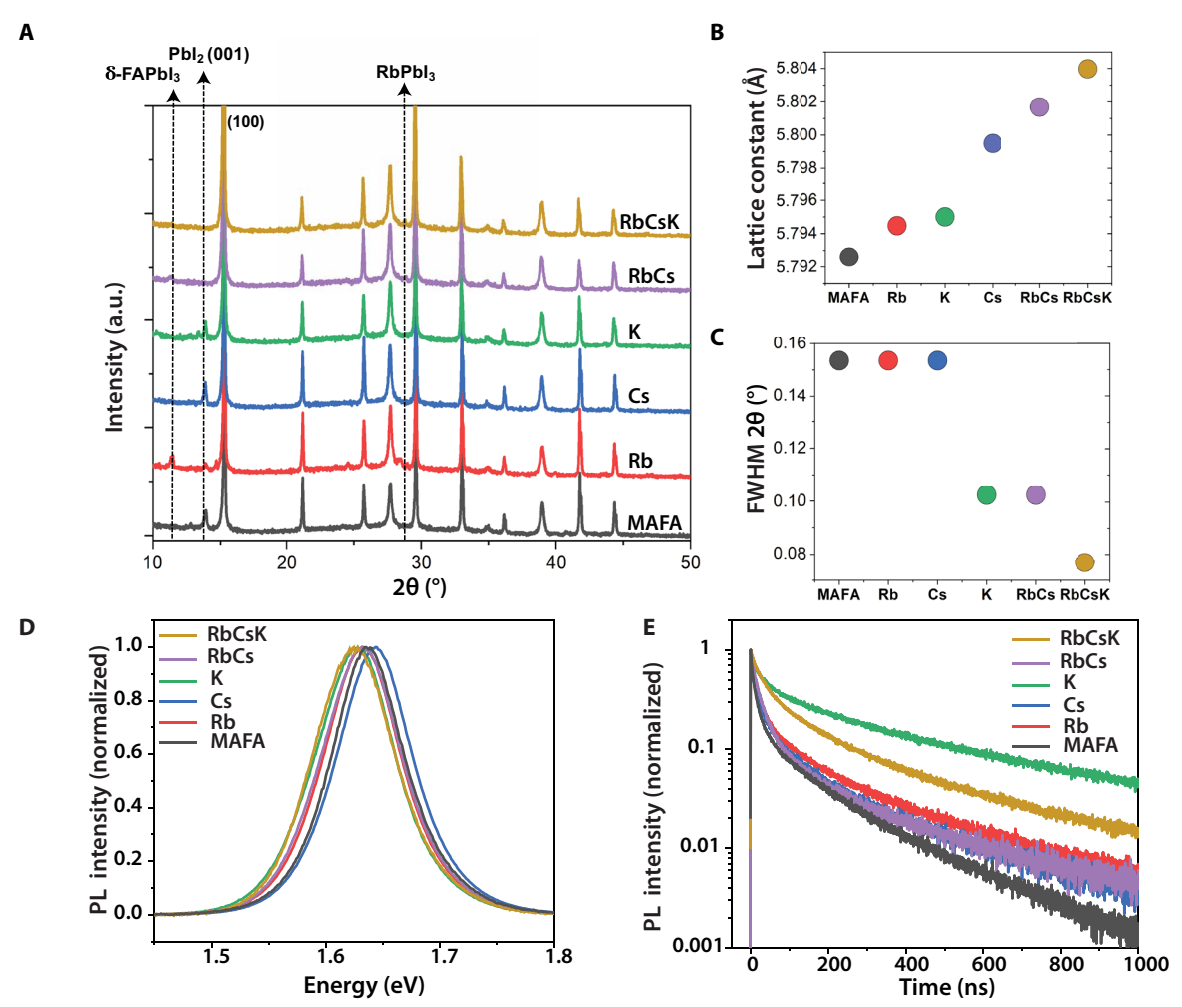


Fig. 1. Structural and optoelectronic properties modulated by alkali cations. (A) XRD patterns, (B) the lattice constants, and (C) the FWHM of the perovskite peak. The lattice constants and FWHM were extracted from the peak at around 14°. a.u., arbitrary unit. (D) Steady-state PL spectra. (E) Time-resolved PL decay curves for samples with different cation combinations. Elongation of PL lifetime is observed with the addition of alkali cations.

We performed x-ray diffraction (XRD) measurements to investigate the structural changes induced by the addition of the alkali cations (Fig. 1A). The FAPbI<sub>3</sub> perovskite δ phase, detrimental for optoelectronic applications, is present for the RbMAFA and RbCsMAFA samples and has been reported for the MAFA samples previously (24), as evident from the peaks around 12°. The  $\delta$  phase is suppressed when adding K<sup>+</sup>, as shown for RbCsKMAFA and KMAFA. However, it is possible that the  $\delta$  phase is present for some of these compounds without showing a peak because not all orientations are detectable by thin-film XRD. In addition, the PbI<sub>2</sub> (001) peak disappears when mixed alkali metals are present, as evidenced by the decrease in the peak around 12.7°. We calculated the lattice constants from the perovskite peak at around 14° and observed an increase when adding alkali metals with the largest increase for RbCsKMAFA (Fig. 1B). While the incorporation of Rb or K in the structure is still under debate, the expanded lattices suggest the incorporation of the alkali metals at the A site, the large X site halide, or both (25). To accommodate the cations while maintaining an overall cubic symmetry, the positions of I and Br across the lattices could also be modified. Full width at half maximum (FWHM) from the perovskite peak at around 14° is the smallest for the RbCsKMAFA perovskite, which can be explained

by increased crystallite size. All the compositions investigated display similar bandgaps at around 1.6 eV, as shown in the steady-state photoluminescence (PL) spectra (Fig. 1D) and absorption spectra (fig. S1B), with small shifts in energy consistent with a previous report (25).

We also used x-ray fluorescence (XRF) microscopy to map the distribution of the different inorganic components of the perovskite films. The elemental distribution for the Br-to-Pb ratio, Rb, and K maps are illustrated in fig. S1C. Rb<sup>+</sup> and Cs<sup>+</sup> homogenize the bromine aggregates compared with the MAFA samples, which is beneficial for solar cell performance and stability (6). However, the presence of Rb<sup>+</sup> also leads to needle-like Rb agglomerates. The addition of K to RbCsMAFA leads to halide homogenization and lower concentration of Rb clusters. Time-resolved PL measurements were carried out to investigate how the interband recombination of cooled carriers is affected by the alkali cations (Fig. 1E). Overall, the addition of Rb<sup>+</sup>, Cs<sup>+</sup>, and K<sup>+</sup> increases the PL lifetime, with the longest PL lifetime observed in KMAFA, consistent with previous reports (6, 21, 23, 25). Furthermore, the recombination on the short time scale (fig. S1D) is suppressed most notably when all three cations are incorporated in RbCsK.

# Carrier cooling modulated by alkali cations

Hot carrier cooling dynamics in different multication perovskite thin films was characterized using TA spectroscopy with identical experimental conditions for the measurements on different samples. Carrier cooling can be substantially modified by incorporating a small amount of alkali cations. Figure 2 (A and B) shows the timedependent TA spectra of MAFA and RbCsMAFA with a pump photon energy of 3.10 eV, respectively. Upon photoexcitation, a ground-state bleach band (GSB, positive signal in  $\Delta T/T$ , where  $\Delta T$  is pump-induced change in probe transmission and T is the probe transmission) centered around the bandgap at 1.64 eV is observed due to the band-filling effect. As schematically illustrated in fig. S2A, carrier-carrier scattering events rapidly distribute initial nonequilibrium carriers into a Fermi-Dirac distribution, which can be described by an effective temperature. Carrier thermalization occurs on a time scale of 85 fs (26), which is beyond our time resolution of ~200 fs. The broad highenergy bleach tails observed in Fig. 2 (A and B) represent the Fermi-Dirac distribution, and they gradually narrow as the carriers cool down. A photoinduced absorption (negative signal in  $\Delta T/T$ ) band near 1.58 eV is also observed at delay time shorter than 1 ps, which has been assigned to bandgap renormalization due to hot carriers (8, 9). At a very short time scale, the trade-off from bandgap renormalization (red shift) and Burstein-Moss effect (blue shift) causes a slightly red-shifted GSB peak.

The incorporation of alkali cations leads to broader higher-energy tails at 200 fs (fig. S2B). We extracted the effective carrier temperature  $T_{\rm c}$  to describe the quasi-equilibrium distribution of the hot carriers.  $T_{\rm c}$  is obtained by fitting the high-energy bleach tail above the bandgap with the Maxwell-Boltzmann distribution (10)

$$\frac{\Delta T}{T}(\hbar\omega) = A_0(\hbar\omega) \exp\left(-\frac{\hbar\omega}{k_{\rm B}T_{\rm c}}\right) \tag{1}$$

where  $\hbar\omega$  is the probe energy,  $A_0$  is the linear absorbance, and  $k_{\rm B}$  is the Boltzmann constant. To ensure the carrier distributions can be defined by an effective temperature, we extracted  $T_{\rm c}$  after carrier thermalization (26) at a time delay of 200 fs or longer. Fig. 2 (C and D) shows the fitting results at different injected carrier density  $N_0$  for MAFA and RbCsKMAFA, respectively. To account for the slight variation in the bandgap energy of different compositions, we fitted the data from different samples at 0.05 eV above their respective bleach maximum at 850 ps (after carrier cooling has concluded). Shifting the fitting window slightly ( $\sim$ 0.03 eV) does not change  $T_{\rm c}$  substantially as shown in fig. S2C. Carrier cooling curves from different samples at  $N_0$  of  $1.3 \times 10^{18}$  cm<sup>-3</sup> are compared in Fig. 2E.

Carrier temperature can be increased by the incorporation of alkali cations. Adding Cs<sup>+</sup> increases the initial carrier temperature slightly to ~700 K in comparison with that of ~640 K for MAFA with overall similar cooling behaviors. Carrier temperature is enhanced more notably by the addition of Rb<sup>+</sup> and K<sup>+</sup>, increasing initial  $T_c$  to ~800 and ~ 950 K, respectively. Carrier temperature is further elevated when multiple alkali cations are incorporated. When both Rb<sup>+</sup> and Cs<sup>+</sup> are incorporated, RbCsMAFA exhibits higher initial  $T_c$  compared with both RbMAFA and CsMAFA. The highest  $T_c$  is achieved when all three alkali cations are incorporated in RbCsKMAFA, ~1500 K at  $N_0$  of  $1.3 \times 10^{18}$  cm<sup>-3</sup>, and ~5000 K at  $N_0$  of  $3.0 \times 10^{18}$  cm<sup>-3</sup> at 200 fs. There could be fitting errors due to the convolution of the GSB peak with the Maxwell-Boltzmann distribution given by Eq. 1 (27). However, the variations in the peak width do not explain the trend observed in Fig. 2E, as RbCsKMAFA (the highest  $T_c$ ) and MAFA (the lowest  $T_c$ ) have similar FWHM for GSB peak as shown in fig. S2D. In contrast, CsMAFA has the largest FWHM but the second lowest  $T_{\rm c}$ . We also quantified the effect of peak width in the temperature fitting by comparing  $T_c$  from Eq. 1 with  $T_c$  obtained from the fitting to the convolution of Eq. 1 with a Gaussian peak shape as described in (27) (more details in note S1A). These two methods yield the same

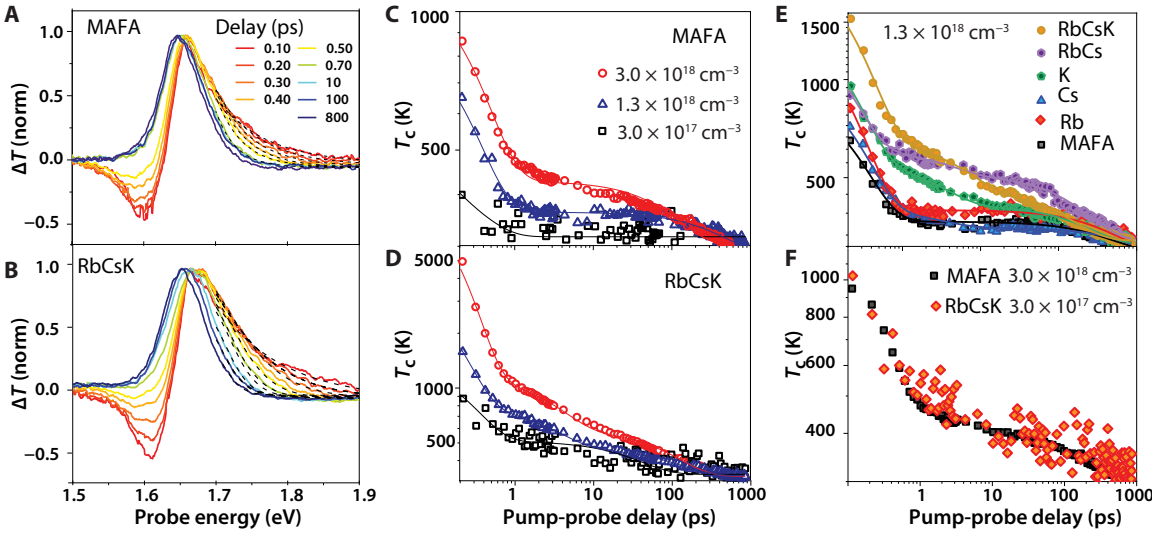


**Fig. 2. Hot carrier cooling modulated by alkali cations.** (**A** and **B**) Normalized TA spectra of pump at 3.10 eV with excitation density of  $1.3 \times 10^{18}$  cm<sup>-3</sup> at different pump-probe delays for MAFA (A) and RbCsKMAFA (B), respectively. Spectral broadening at early delay time indicates hot carrier distributions. The black dashed lines are fits to the high-energy bleach tail with the Maxwell-Boltzmann distribution to extract effective carrier temperature  $T_c$ , as described in the main text. (**C** and **D**) Extracted  $T_c$  of MAFA and RbCsKMAFA as a function of delay time at different carrier densities. (**E**) Carrier cooling curves for different samples at  $N_0$  of  $1.3 \times 10^{18}$  cm<sup>-3</sup>, displaying strong dependence on alkali cations. (**F**) Similar initial  $T_c$  and cooling behavior can be achieved in RbCsKMAFA with an order of magnitude lower  $N_0$  than the reference MAFA  $(3 \times 10^{17} \text{ versus } 3 \times 10^{18} \text{ cm}^{-3})$ . Solid lines are the fitted with biexponential or triexponential functions, and the fitting parameters are given in table S1.

trend as a function of alkali cations and similar  $T_{\rm c}$  values with a deviation <5% (fig. S3), indicating the broadening from the GSB peak width does not substantially affect the extracted  $T_{\rm c}$ . Furthermore, we have extracted  $T_{\rm c}$  by fitting the whole TA spectra using the model described in (10, 28) that considers Fermi-Dirac distribution of the carriers, broadening of the exciton and free carrier transitions, and bandgap renormalization effects (fig. S4 and note S1B). The temperatures extracted from these fits are within 14% of the fits from the Maxwell-Boltzmann method with the same trend as a function of alkali cations. Therefore, all three fitting models yield overall similar results, which confirms that the approximation to a Maxwell-Boltzmann distribution is valid for our experimental conditions.

Carrier cooling can be roughly divided into two regimes, with a fast subpicosecond cooling and slow cooling ranging from picoseconds to hundreds of picoseconds (7, 9-11, 13, 26). For the subpicosecond time scale, before the formation of polarons, the cooling of the hot bare carriers is dominated by the emission of the optical phonon via the Fröhlich mechanism. Fitting of carrier cooling in the subpicosecond regime returned fast decay constants of 200 to 300 fs for all samples. Additional slower cooling stages are observed with decay time up to hundreds of picoseconds at sufficiently high carrier densities (Fig. 2, C and D, and fig. S5), which is attributed to the hot phonon bottleneck effect (9-13, 29). The bottleneck occurs when the emission of optical phonons (12, 30) builds up a nonequilibrium phonon population that can transfer energy back to the electron system. The addition of K<sup>+</sup> and Rb<sup>+</sup> lowers the carrier density threshold for the phonon bottleneck, leading to slow picosecond cooling at density as low as  $3 \times 10^{17}$  cm<sup>-3</sup> (the slow cooling is absent from MAFA and CsMAFA at this carrier density as illustrated in fig. S5). Similar initial  $T_c$  and cooling behavior can be achieved in RbCsKMAFA with an order of magnitude lower  $N_0$  compared with the reference MAFA as shown in Fig. 2F  $(3 \times 10^{17} \text{ cm}^{-3} \text{ versus})$  $3 \times 10^{18}$  cm<sup>-3</sup>). When the initial carrier temperature is ~1000 K or above and most notably with the incorporation of K<sup>+</sup>, a third exponential term with time constant of 3 to 7 ps is necessary to describe the cooling, possibly due to an additional relaxation pathway for the optical phonons (Fig. 2E). This additional decay leads to a higher  $T_c$ in RbCsMAFA than in RbCsKMAFA at delays >10 ps. The fitting parameters for the cooling curves shown in Fig. 2 and fig. S5 are given in table S1. Auger heating has also been proposed to contribute to the slow carrier cooling (13). However, Auger recombination would also lead to additional loss of carrier population. As shown in fig. S6, carrier dynamics is independent of carrier density for  $N_0$ ranging from  $3 \times 10^{17}$  to  $3 \times 10^{18}$  cm<sup>-3</sup>, suggesting negligible Auger annihilation. Therefore, we conclude that phonon bottleneck is the dominant mechanism for the slow carrier cooling observed here.

The large difference in the initial  $T_c$  and subsequent cooling processes between different samples indicates that energy loss (inelastic) carrier scattering events within 200 fs are altered by the addition of the alkali cations. These processes could include carrier defect or carrier impurity scattering that occurs on the time scales of 200 fs or shorter (31). The alkali cations also reduce the threshold carrier density for hot phonon effects, because the loss of excessive energy to defects is suppressed. Cs<sup>+</sup> can replace the MA<sup>+</sup> or FA<sup>+</sup> in the perovskite structure and can be found homogeneously within the material (32), but the smaller Rb<sup>+</sup> and K<sup>+</sup> do not substitute the organic cations. Cs<sup>+</sup> leads to the least increase in  $T_c$ , suggesting that the suppressed scattering is likely not due to replacing MA or FA. Overall, highest  $T_c$  is achieved in RbCsKMAFA, implying synergetic effects

from the three cations. At a time scale of 200 fs or shorter, structural changes at the localized nanometer length scale are expected to play a more important role than the hundreds of nanometer to micrometer morphology variations. From the XRD results, RbCsKMAFA and RbCsMAFA exhibit the most expansion of the lattice and the sharpest (100) diffraction peaks (Fig. 1, B and C), which are the signatures of relaxed local strain, as previously shown in hybrid perovskite structures after light soaking (33). Lattice strains can lead to energy fluctuations or structural defects locally on the nanometer scale, which could serve as additional scattering centers for hot carriers. For example, local lattice strains have been shown to lead to additional hot carrier scattering pathways that accelerate carrier cooling in semiconducting quantum wells (34). Thus, it is possible that relaxation of local strain by the alkali cations reduces hot carrier scattering and leads to increased  $T_{\rm c}$ .

The addition of the alkali cations has also been suggested to passivate other structural defects such as halide vacancies (20-23). The role of defects in quenching hot carrier temperature has been implied previously by the cooler carriers at grain boundaries with presumably higher defect density as revealed by spatially resolved TA measurements (35). The fact that KMAFA displays a substantially higher  $T_c$  than RbMAFA and CsMAFA is consistent with that K<sup>+</sup> was proposed to be more effective in passivating halide vacancies (20). Compensating the halide vacancies could also lead to the shifting of the Fermi level toward the middle of the bandgap (20) and reduce the overall carrier density and carrier-carrier scattering, leading to higher  $T_c$ . In addition, we observed that the PL lifetime at the short time scale (fig. S1D) correlates with initial  $T_c$  shown in Fig. 2E (both in the order of RbCsK > K ~ RbCs > Rb > CS ~ MAFA). This agreement indicates that the defects that lead to the PL recombination at the subnanosecond time scale are the more localized ones that also quench hot carrier temperatures. Note that the Rb agglomerates with sizes >100 nm could lead to recombination on a time scale longer than 10 ns; however, they do not result in substantially detrimental effects in hot carrier scattering at the hundreds of femtosecond time scale, and an improved carrier temperature is observed in RbMAFA compared with MAFA.

# Ab initio calculations of hot carrier scattering by halide vacancies

We use ab initio nonadiabatic (NA) molecular dynamics (MD) (36, 37) simulations to gain further insights into how the localized defects affect the hot carrier cooling process (more details in note S2). Because vacancies can break the continuity of chemical bonding by virtue of both missing atom and missing interatomic linkages, they are expected to be efficient scattering sites. Thus far, the investigation of halide vacancies has been focused exclusively on their effect on the recombination of cooled carriers at the band edge due to defect states within the bandgap (20, 21, 23). Here, we simulated the intraband relaxation of hot carriers in pristine MAPbI<sub>3</sub> and compared it to that in the presence of an iodine vacancy  $(I_v)$ . The simulation details are given in note S1, and the results are presented in Fig. 3. The density of states (DOS) at 300 K shown in Fig. 3 (A and B) demonstrates that I<sub>v</sub> introduces a midgap state, which can lead to additional recombination channels for the cooled carriers and shorter PL lifetimes. I<sub>v</sub> also increases the DOS near the conduction band minimum (CBM), as highlighted in Fig. 3B by the blue oval. The increased DOS near the CBM can influence intraband relaxation, which is relevant for hot carrier cooling. The higher DOS contributes carrier scattering

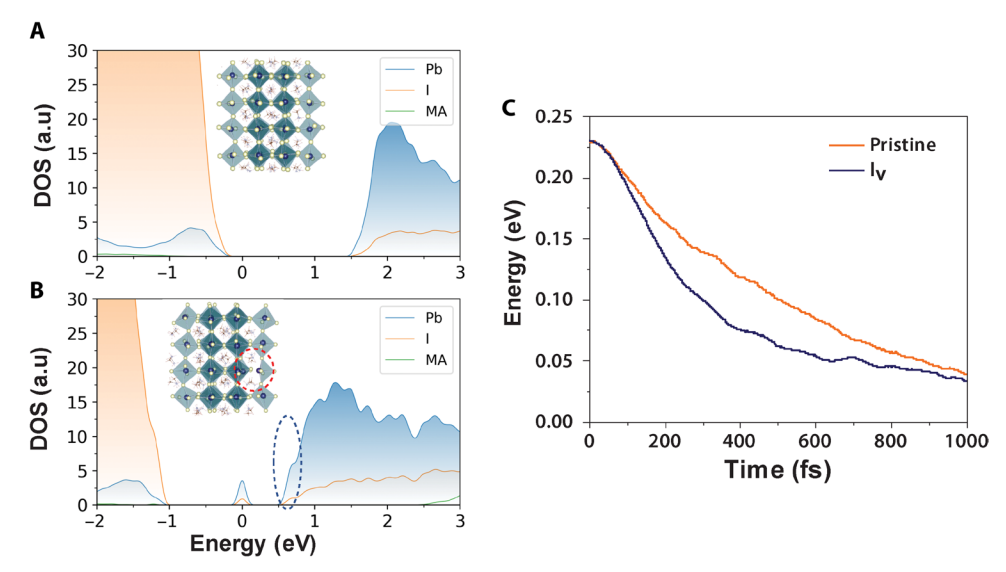


Fig. 3. Ab initio calculations on the effect of  $I_vs$  on carrier cooling. (A and B) Atom-projected DOS for pristine MAPbI<sub>3</sub> (A) and lattice with  $I_v$  (B) for representative structures at 300 K. The zero of energy is at the Fermi level. The insets show atomic structures, with the red circle indicating the defect location. The  $I_v$  introduces a strong peak in the DOS near the CBM, highlighted with the blue oval. The increased DOS accelerates hot electron cooling. (C) Hot electron relaxation. The relaxation is accelerated by  $I_v$  due to the increased DOS near the CBM.

pathways, which can lead to a lower initial carrier temperature and faster cooling (Fig. 3C).

In addition to the higher DOS, the states near the vacancies are more localized (fig. S7). Typically, electron-phonon coupling is stronger for localized electronic states. For instance, excitation of localized molecular states can lead to large Stokes shifts and bond breaking, while excitation of delocalized states in bulk materials has little influence on their geometries and phonon frequencies. The localization of the electronic states in the presence of  $\rm I_v$  increases the NA electron-phonon coupling and accelerates electron-phonon relaxation and hot carrier cooling. Overall, the NA MD calculation presents a feasible explanation for how the addition of alkali cations modify intraband relaxation and hot carrier dynamics by passivating the halide vacancies.

# Enhancing hot carrier transport by alkali cations

Long-range transport is also necessary for the success of hot carrier solar cells in addition to the need of preserving carrier temperature. Here, we used TA microscopy (TAM) to directly image the transport of the hot carrier population protected by alkali metal cations. To image carrier transport, we held the pump beam at a fixed position, while the probe beam is scanned relative to the pump with a Galvanometer scanner, and  $\Delta T$  is plotted as a function of probe position to form an image (fig. S8; more details in Materials and Methods and note S3) (38). The probe is at 1.65 eV resonant with the bandgap. The initial population is created by a Gaussian pump beam at position  $(x_0, y_0)$  with a pulse duration of ~300 fs,  $n(x, y, 0) = N \exp \left[ -\frac{(x-x_0)^2}{2\sigma_{0,x}^2} - \frac{(y-y_0)^2}{2\sigma_{0,y}^2} \right]$ . The time-dependent TAM images reflect carrier diffusion away from the initial excitation volume. The resulting two-dimensional

(2D) TAM images are shown in Fig. 4A for a pump photon energy of 3.10 eV at  $N_0 = 5.0 \times 10^{17}$  cm<sup>-3</sup> for the RbCsKMAFA thin film

(and the images for MAFA and RbCsMAFA are shown in fig. S9, A

and B, respectively). The TAM profiles shown in Fig. 4A are fitted by 2D Gaussian functions with variances of  $\sigma_{t,x}^2$  and  $\sigma_{t,y}^2$ , where  $\sigma_{t,x}^2$  and

the *x* and *y* axes. At delay time *t*, the carrier population is given by  $n(x,y,t) = N \exp\left[-\frac{(x-x_0)^2}{2\sigma_{t,x}^2} - \frac{(y-y_0)^2}{2\sigma_{t,x}^2}\right]$ . The Gaussian fits along one direction are shown in Fig. 4B (the Gaussian profiles for MAFA and RbCsMAFA are shown in fig. S9, A and B, respectively). Because the carrier transport is isotropic,  $\sigma_{t,x}^2 = \sigma_{t,y}^2 = \sigma_t^2$  (8).  $\sigma_t^2 - \sigma_0^2$  represents the average distance traveled by the carriers during delay time *t*. For the transport measurements, the critical resolution of TAM of ~50 nm comes from the uncertainty of  $\sigma_t$  and  $\sigma_0$ , which is limited by the signal-to-noise rather than the diffraction limit (more details in note S3) (38).

 $\sigma_{t,y}^2$  are the time-dependent variances of the Gaussian profiles along

The TAM results show a two-step transport behavior: enhanced transport of the hot carriers during early delay time and normal diffusion of the cooled carriers at later time (Fig. 4). Enhanced hot carrier transport was observed to correlate with higher carrier temperature induced by alkali cation incorporation, beneficial for hot solar cell applications. We compared hot carrier transport at a  $N_0$  of  $5.0 \times 10^{17}$  cm<sup>-3</sup> in the two compositions that are most promising for hot carrier solar cell applications, RbCsMAFA and RbCsKMAFA, to that in MAFA (Fig. 4C). At early delay time, the transport of the carriers in both RbCsKMAFA and RbCsMAFA with higher  $T_c$  is more rapid than the carriers in MAFA (Fig. 4C). Hot carriers migrated the largest distance in RbCsKMAFA, ~230 nm greater than MAFA and ~200 nm greater than RbCsMAFA (by subtracting the difference in  $\sigma_{150 \text{ ps}}^2$  in Fig. 4C). Note that hot carrier transport on the subpicosecond time scales in hybrid perovskites is dominated by quasi-ballistic transport of hot bare band carriers, and carrier propagation has occurred within the pulse duration of ~300 fs, leading to a  $\sigma_0^2$  value larger than the convolution of the pump and probe beams (8, 39). The highest initial  $T_c$  in RbCsKMAFA results in the longest-range quasi-ballistic carrier migration within the pulse duration, as demonstrated by the largest  $\sigma_0^2$  value (Fig. 4C). The diffusion constant of the thermally equilibrated cooled carriers at time scale >500 ps is lower in RbCsKMAFA

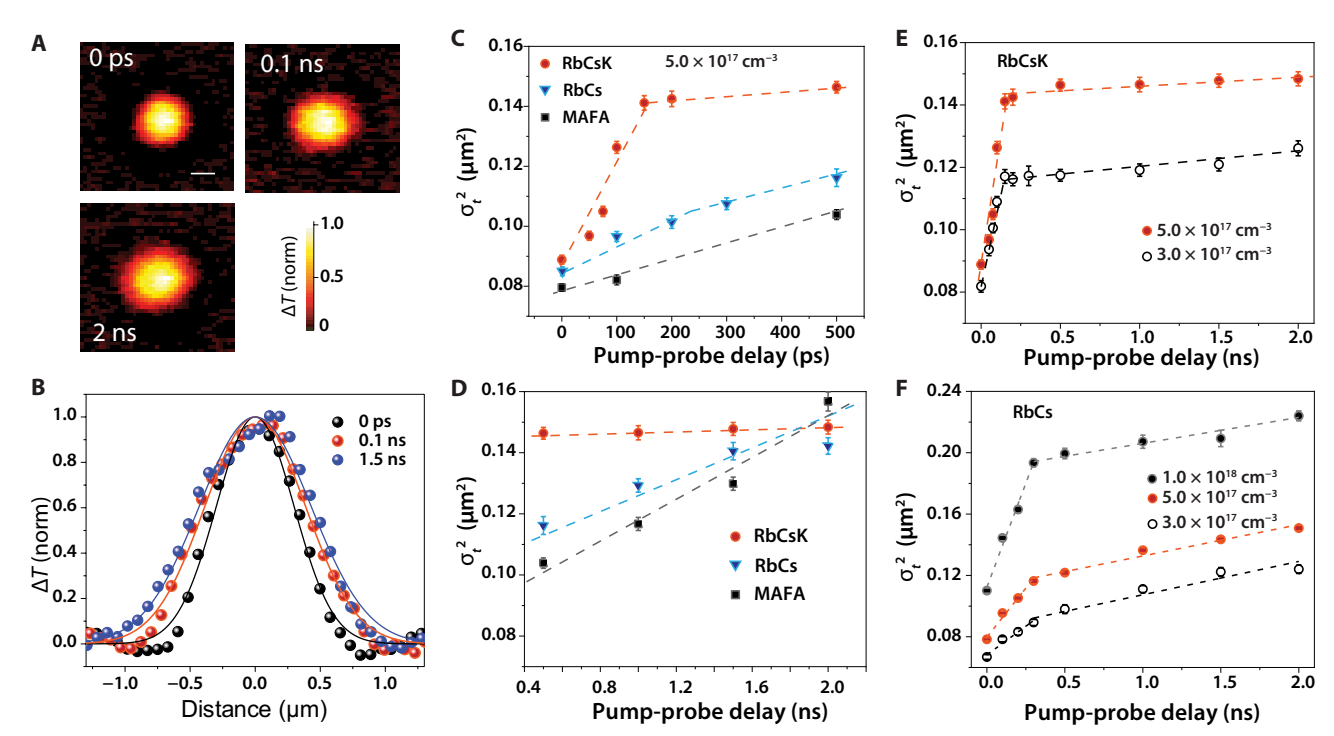


**Fig. 4. Enhancing hot carrier transport by alkali cations.** (**A**) The TAM images of the carrier transport in RbCsKMAFA at various delay times. Probe energy = 1.65 eV, pump energy = 3.10 eV, and  $N_0 = 5.0 \times 10^{17}$  cm<sup>-3</sup>. The color scale represents the intensity of pump-induced differential transmission (Δ*T*) of the probe, and every image has been normalized by peak value. Scale bar, 500 nm. (**B**) Cross sections of the TAM images shown in (A) fitted with Gaussian functions, with the maximum Δ*T* signal normalized. (**C**)  $\sigma_t^2$  plotted as a function of pump-probe delay time, comparing hot carrier transport in MAFA, RbCsMAFA, and RbCsKMAFA. Probe energy = 1.65 eV. The dashed lines are guide to the eye. More rapid hot carrier transport is observed in RbCsMAFA and RbCsKMAFA than in MAFA. The error bars of  $\sigma_t^2$  indicate the uncertainties of the Gaussian fitting. (**D**) Transport of cooled carriers;  $\sigma_t^2$  at time delay >500 ps for MAFA, RbCsMAFA, and RbCsKMAFA at  $N_0 = 5.0 \times 10^{17}$  cm<sup>-3</sup>. (**E** and **F**) Longer-range hot carrier transport is observed at higher carrier density for RbCsKMAFA (E) and RbCsMAFA (F).  $\sigma_t^2$  plotted as a function of pump-probe delay time under different excitation densities.

than in MAFA ( $0.02 \text{ cm}^2 \text{ s}^{-1} \text{ versus } 0.18 \text{ cm}^2 \text{ s}^{-1}$ ) as shown in Fig. 4D. Therefore, we can exclude better mobility in RbCsKMAFA as the reason for the enhanced transport of the hot carriers.

The enhanced hot carrier transport is consistent with the higher  $T_c$  in RbCsKMAFA and RbCsMAFA than in MAFA as shown in Fig. 2E and can be explained by that a higher  $T_c$  leads to a larger velocity of the carriers as given by  $v = \sqrt{\frac{3k_BT_c}{m^*}}$ , where  $m^*$  is the effective

mass. Under the same carrier density, hot carriers propagate shorter distance in RbCsMAFA than in RbCsKMAFA because of lower carrier temperature in RbCsMAFA (Fig. 2D and fig. S5D). Hot carrier transport can be further enhanced by increasing carrier density. Faster transport is observed for RbCsKMAFA and RbCsMAFA at higher carrier density (shown in Fig. 4, E and F, respectively), again consistent with higher carrier temperature at a large  $N_0$  due to hot phonon effect (Fig. 2D and fig. S5D). Because the density is higher at the center of the spot than at the edge of the Gaussian pump beam, leading to faster decay due to Auger annihilation, annihilation could lead to artificial broadening of  $\sigma$  at higher carrier density. We rule out the influence of Auger annihilation here based on the negligible carrier density-dependent recombination as shown in fig. S6. The variation of the carrier density within the Gaussian pump beam could also lead to spatially dependent carrier cooling. To fully address this spatial dependence, a detailed Monte Carlo simulation that takes into account both the cooling and transport processes is necessary, which is beyond the scope of this work. Instead, here, we

interpret the TAM results as the averaged transport behaviors of all the excited carriers.

The enhanced transport persists for longer time in RbCsMAFA than in RbCsKMAFA (~300 versus ~150 ps; Fig. 4, E and F), consistent with a slower carrier cooling process in RbCsMAFA (Fig. 2E). The two-step transport transition time point correlates with the cooling time of 220 and 150 ps for RbCsMAFA and RbCsKMAFA at an excitation density of  $1.3 \times 10^{18}$  cm<sup>-3</sup>, respectively (table S1). This correlation of the duration of enhanced transport with the carrier cooling time provides additional support for hot carrier diffusion. While small spatial variations in the diffusion constants are observed, similar time-dependent transport behaviors are reproducible among different sample locations (fig. S10). The SD for  $\sigma_t^2 - \sigma_0^2$  from multiple datasets is  $\pm 6$  and  $\pm 9\%$  for RbCsMAFA and RbCsKMAFA, respectively.

# **DISCUSSION**

The results presented here highlight the unique advantage of solution-processable hybrid perovskites with programmable structures over other candidates for hot carrier solar cells such as semiconducting quantum wells that require epitaxial growth (40). By simple solution chemistry of adding a small amount of alkali metal halides in the precursors, significant improvement on hot carrier temperature and migration can be achieved. The carrier density required for achieving slow picosecond carrier cooling by hot phonon

effect is also reduced by the alkali cations. X-ray structural characterizations and theory simulations suggest that these improvements result from the combined effects of the relaxation of local strains and the passivation of defects. RbCsKMAFA is the most promising structure with overall highest carrier temperature and longest-range transport obtained, implying the synergetic effects from the Rb<sup>+</sup>, Cs<sup>+</sup>, and K<sup>+</sup> cations. The protected hot carriers in alkali cation–incorporated structures that have demonstrated superior thermal stability (6) suggest that these structures are practical for hot carrier applications. At a carrier density of  $\sim 10^{18}$  cm<sup>-3</sup> ( $\sim 100$  sun, can be achieved using solar concentrator), carrier temperature greater than 600 K can be maintained over a time scale of >10 ps and a distance over hundreds of nanometers, which has the potential for achieving a PCE >45% in a hot carrier solar cell (1).

### **MATERIALS AND METHODS**

# Sample preparation and structural characterization

The preparation and structural characterizations (XRD and XRF mapping) of the perovskite thin films are based on methods described previously (6). The alkali metal iodides were added as CsI, RbI, and KI in 5% molar ratios of the alkali metal to the precursor solution of MAFA.

### PL measurements

A homebuilt microscope was used for the PL and time-resolved PL spectroscopy measurements. A picosecond pulse laser with wavelength of 447 nm was used as the excitation, and an objective  $(40\times, \text{numerical aperture} = 0.6, \text{Nikon})$  was used to focus the excitation light on the sample and collect the epic scattered PL emission. A spectrometer and charge-coupled device (CCD) combo (Andor) was used for PL spectral analysis. Time-resolved PL was acquired using a single-photon avalanche diode (PDM series, PicoQuant) and a single-photon counting module (PicoQuant).

# TA spectroscopy

TA spectra of the perovskite thin films were measured by a femto-second pump-probe system with a homebuilt TA spectrometer described in our previous publication (8). Laser pulses at 1030 nm with ~200-fs duration were generated by a 400-kHz amplified Yb:KGW laser system (PHAROS, Light Conversion Ltd.). The probe beam was a white-light continuum beam spanning 450- to 950-nm spectral region, created by focusing 5% of the 1030-nm fundamental output onto a YAG (yttrium aluminum garnet) crystal (4.0 mm thick). The rest of the output pumps an optical parametric amplifier (OPA; TOPAS-Twins, Light Conversion Ltd.) to generate pump pulses at 400 nm (3.1 eV).

# **TA microscopy**

The homebuilt TAM setup used in this study has been described in our previous publication (8). Briefly, the output from two independent OPAs (400 kHz and  $\sim$  200 fs; Light Conversion) served as the pump and probe beam, respectively, which were focused on a sample with an objective ( $60\times$ , numerical aperture = 0.95, Nikon). An acousto-optic modulator (Gooch and Housego, R23080-1) triggered by a lock-in amplifier (SR830, Stanford Research Systems Inc.) was used to modulate the pump beam. A mechanical translation stage (Thorlabs, DDS600-E) was used to delay the probe with respect to the pump. A 2D galvo mirror (Thorlabs GVS012) was used to scan the

probe beam relative to the pump beam in space (path 1 in fig. S8). Spatial filters were used to optimize the profile of the pump and probe beams. The transmitted probe light was detected by an avalanche photodiode (Hamamatsu, C5331-04). The pump-induced change in the probe reflection ( $\Delta T$ ) was extracted by the lock-in amplifier.

# Time-dependent density functional theory calculations

The ab initio NA MD simulations were performed using the PYXAID code (37) within the framework of the real-time time-dependent density functional theory (DFT) in the Kohn-Sham representation (36).

### **SUPPLEMENTARY MATERIALS**

Supplementary material for this article is available at http://advances.sciencemag.org/cgi/content/full/6/43/eabb1336/DC1

# **REFERENCES AND NOTES**

- 1. A. J. Nozik, Utilizing hot electrons. Nat. Energy 3, 170-171 (2018).
- W. Shockley, H. J. Queisser, Detailed balance limit of efficiency of p-n junction solar cells. J. Appl. Phys. 32. 510–519 (1961).
- G. Conibeer, N. Ekins-Daukes, J.-F. Guillemoles, D. König, E.-C. Cho, C.-W. Jiang, S. Shrestha, M. Green, Progress on hot carrier cells. Sol. Energy Mater. Sol. Cells 93, 713–719 (2009).
- M. M. Lee, J. Teuscher, T. Miyasaka, T. N. Murakami, H. J. Snaith, Efficient hybrid solar cells based on meso-superstructured organometal halide perovskites. *Science* 338, 643–647 (2012)
- D. P. McMeekin, G. Sadoughi, W. Rehman, G. E. Eperon, M. Saliba, M. T. Hörantner, A. Haghighirad, N. Sakai, L. Korte, B. Rech, M. B. Johnston, L. M. Herz, H. J. Snaith, A mixed-cation lead mixed-halide perovskite absorber for tandem solar cells. Science 351, 151–155 (2016).
- J.-P. Correa-Baena, Y. Luo, T. M. Brenner, J. Snaider, S. Sun, X. Li, M. A. Jensen, N. T. P. Hartono, L. Nienhaus, S. Wieghold, J. R. Poindexter, S. Wang, Y. S. Meng, T. Wang, B. Lai, M. V. Holt, Z. Cai, M. G. Bawendi, L. Huang, T. Buonassisi, D. P. Fenning, Homogenized halides and alkali cation segregation in alloyed organic-inorganic perovskites. *Science* 363, 627–631 (2019).
- H. Zhu, K. Miyata, Y. Fu, J. Wang, P. P. Joshi, D. Niesner, K. W. Williams, S. Jin, X.-Y. Zhu, Screening in crystalline liquids protects energetic carriers in hybrid perovskites. Science 353, 1409–1413 (2016).
- Z. Guo, Y. Wan, M. Yang, J. Snaider, K. Zhu, L. Huang, Long-range hot-carrier transport in hybrid perovskites visualized by ultrafast microscopy. Science 356, 59–62 (2017).
- M. B. Price, J. Butkus, T. C. Jellicoe, A. Sadhanala, A. Briane, J. E. Halpert, K. Broch, J. M. Hodgkiss, R. H. Friend, F. Deschler, Hot-carrier cooling and photoinduced refractive index changes in organic-inorganic lead halide perovskites. *Nat. Commun.* 6, 8420 (2015).
- Y. Yang, D. P. Ostrowski, R. M. France, K. Zhu, J. van de Lagemaat, J. M. Luther, M. C. Beard, Observation of a hot-phonon bottleneck in lead-iodide perovskites. *Nat. Photonics* 10, 53–59 (2016).
- J. Yang, X. Wen, H. Xia, R. Sheng, Q. Ma, J. Kim, P. Tapping, T. Harada, T. W. Kee, F. Huang, Y.-B. Cheng, M. Green, A. Ho-Baillie, S. Huang, S. Shrestha, R. Patterson, G. Conibeer, Acoustic-optical phonon up-conversion and hot-phonon bottleneck in lead-halide perovskites. *Nat. Commun.* 8, 14120 (2017).
- D. M. Monahan, L. Guo, J. Lin, L. Dou, P. Yang, G. R. Fleming, Room-temperature coherent optical phonon in 2D electronic spectra of CH<sub>3</sub>NH<sub>3</sub>Pbl<sub>3</sub> perovskite as a possible cooling bottleneck. *J. Phys. Chem. Lett.* 8, 3211–3215 (2017).
- J. Fu, Q. Xu, G. Han, B. Wu, C. H. A. Huan, M. L. Leek, T. C. Sum, Hot carrier cooling mechanisms in halide perovskites. *Nat. Commun.* 8, 1300 (2017).
- 14. K. Miyata, T. L. Atallah, X.-Y. Zhu, Lead halide perovskites: Crystal-liquid duality, phonon glass electron crystals, and large polaron formation. *Sci. Adv.* **3**, e1701469 (2017).
- J. M. Frost, L. D. Whalley, A. Walsh, Slow cooling of hot polarons in halide perovskite solar cells. ACS Energy Lett. 2, 2647–2652 (2017).
- K. K. Ng, C.-S. Pai, W. M. Mansfield, G. A. Clarke, Suppression of hot-carrier degradation in Si MOSFETs by germanium doping. *IEEE Electron Dev. Lett.* 11, 45–47 (1990)
- J. Mao, J. Shuai, S. Song, Y. Wu, R. Dally, J. Zhou, Z. Liu, J. Sun, Q. Zhang, C. dela Cruz, S. Wilson, Y. Pei, D. J. Singh, G. Chen, C.-W. Chu, Z. Ren, Manipulation of ionized impurity scattering for achieving high thermoelectric performance in n-type Mg<sub>3</sub>Sb<sub>2</sub>-based materials. *Proc. Natl. Acad. Sci. U.S.A.* 114, 10548–10553 (2017).

# SCIENCE ADVANCES | RESEARCH ARTICLE

- M. Saliba, T. Matsui, K. Domanski, J.-Y. Seo, A. Ummadisingu, S. M. Zakeeruddin, J.-P. Correa-Baena, W. R. Tress, A. Abate, A. Hagfeldt, M. Grätzel, Incorporation of rubidium cations into perovskite solar cells improves photovoltaic performance. *Science* 354, 206–209 (2016).
- M. Abdi-Jalebi, Z. Andaji-Garmaroudi, A. J. Pearson, G. Divitini, S. Cacovich, B. Philippe, H. Rensmo, C. Ducati, R. H. Friend, S. D. Stranks, Potassium- and rubidium-passivated alloyed perovskite films: Optoelectronic properties and moisture stability. ACS Energy Lett. 3, 2671–2678 (2018).
- M. Abdi-Jalebi, Z. Andaji-Garmaroudi, S. Cacovich, C. Stavrakas, B. Philippe, J. M. Richter, M. Alsari, E. P. Booker, E. M. Hutter, A. J. Pearson, S. Lilliu, T. J. Savenije, H. Rensmo, G. Divitini, C. Ducati, R. H. Friend, S. D. Stranks, Maximizing and stabilizing luminescence from halide perovskites with potassium passivation. *Nature* 555, 497–501 (2018).
- Y. Hu, E. M. Hutter, P. Rieder, I. Grill, J. Hanisch, M. F. Aygüler, A. G. Hufnagel, M. Handloser, T. Bein, A. Hartschuh, K. Tvingstedt, V. Dyakonov, A. Baumann, T. J. Savenije, M. L. Petrus, P. Docampo, Understanding the role of cesium and rubidium additives in perovskite solar cells: Trap states, charge transport, and recombination. *Adv. Energy Mater.* 8, 1703057 (2018).
- L. Qiao, W.-H. Fang, R. Long, O. V. Prezhdo, Extending carrier lifetimes in lead halide perovskites with alkali metals by passivating and eliminating halide interstitial defects. *Angew. Chem.* 132, 4714–4720 (2019).
- A. Solanki, P. Yadav, S.-H. Turren-Cruz, S. S. Lim, M. Saliba, T. C. Sum, Cation influence on carrier dynamics in perovskite solar cells. *Nano Energy* 58, 604–611 (2019).
- M. Saliba, T. Matsui, J.-Y. Seo, K. Domanski, J.-P. Correa-Baena, M. K. Nazeeruddin,
  M. Zakeeruddin, W. Tress, A. Abate, A. Hagfeldt, M. Grätzel, Cesium-containing triple cation perovskite solar cells: Improved stability, reproducibility and high efficiency. Energy Environ. Sci. 9, 1989–1997 (2016).
- Z. Tang, S. Uchida, T. Bessho, T. Kinoshita, H. Wang, F. Awai, R. Jono, M. M. Maitani, J. Nakazaki, T. Kubo, H. Segawa, Modulations of various alkali metal cations on organometal halide perovskites and their influence on photovoltaic performance. *Nano Energy* 45, 184–192 (2018).
- J. M. Richter, F. Branchi, F. V. de Almeida Camargo, B. Zhao, R. H. Friend, G. Cerullo, F. Deschler, Ultrafast carrier thermalization in lead iodide perovskite probed with twodimensional electronic spectroscopy. *Nat. Commun.* 8, 376 (2017).
- K. J. Savill, M. T. Klug, R. L. Milot, H. J. Snaith, L. M. Herz, Charge-carrier cooling and polarization memory loss in formamidinium tin triiodide. J. Phys. Chem. Lett. 10, 6038–6047 (2019)
- 28. J. W. M. Lim, D. Giovanni, M. Righetto, M. Feng, S. G. Mhaisalkar, N. Mathews, T. C. Sum, Hot carriers in halide perovskites: How hot truly? *J. Phys. Chem. Lett.* **11**, 2743–2750 (2020).
- M. Li, S. Bhaumik, T. W. Goh, M. S. Kumar, N. Yantara, M. Grätzel, S. Mhaisalkar, N. Mathews, T. C. Sum, Slow cooling and highly efficient extraction of hot carriers in colloidal perovskite nanocrystals. *Nat. Commun.* 8, 14350 (2017).
- M. Park, A. J. Neukirch, S. E. Reyes-Lillo, M. Lai, S. R. Ellis, D. Dietze, J. B. Neaton, P. Yang,
  S. Tretiak, R. A. Mathies, Excited-state vibrational dynamics toward the polaron in methylammonium lead iodide perovskite. *Nat. Commun.* 9, 2525 (2018).
- B. K. Ridley, Hot electrons in low-dimensional structures. Rep. Prog. Phys. 54, 169–256 (1991).
- B. Philippe, M. Saliba, J.-P. Correa-Baena, U. B. Cappel, S.-H. Turren-Cruz, M. Grätzel,
  A. Hagfeldt, H. Rensmo, Chemical distribution of multiple cation (Rb<sup>+</sup>, Cs<sup>+</sup>, MA<sup>+</sup>, and FA<sup>+</sup>)
  perovskite materials by photoelectron spectroscopy. Chem. Mater. 29, 3589–3596 (2017).
- H. Tsai, R. Asadpour, J.-C. Blancon, C. C. Stoumpos, O. Durand, J. W. Strzalka, B. Chen, R. Verduzco, P. M. Ajayan, S. Tretiak, J. Even, M. A. Alam, M. G. Kanatzidis, W. Nie, A. D. Mohite, Light-induced lattice expansion leads to high-efficiency perovskite solar cells. Science 360, 67–70 (2018).
- 34. T. Smyth, M. Dvorak, M. J. Y. Tayebjee, V. B. Yasarapudi, H. Xia, Y. Feng, Y. Wang, B. Puthen-Veettil, S. Huang, S. Shrestha, S. P. Bremner, T. W. Schmidt, M. Sugiyama,

- G. J. Conibeer, Hot carrier cooling in In<sub>0.17</sub>Ga<sub>0.83</sub>As/GaAs<sub>0.80</sub>P<sub>0.20</sub> multiple quantum wells: The effect of barrier thickness. *IEEE J. Photovoltaics* **6.** 166–171 (2016).
- S. Nah, B. Spokoyny, X. Jiang, C. Stoumpos, C. M. M. Soe, M. G. Kanatzidis, E. Harel, Transient sub-bandgap states in halide perovskite thin films. *Nano Lett.* 18, 827–831 (2018).
- C. F. Craig, W. R. Duncan, O. V. Prezhdo, Trajectory surface hopping in the timedependent Kohn-Sham approach for electron-nuclear dynamics. *Phys. Rev. Lett.* 95, 163001 (2005).
- A. V. Akimov, O. V. Prezhdo, Advanced capabilities of the PYXAID program: Integration schemes, decoherence effects, multiexcitonic states, and field-matter interaction. J. Chem. Theory Comput. 10, 789–804 (2014).
- Z. Guo, J. S. Manser, Y. Wan, P. V. Kamat, L. Huang, Spatial and temporal imaging of long-range charge transport in perovskite thin films by ultrafast microscopy. *Nat. Commun.* 6, 7471 (2015).
- J. Sung, C. Schnedermann, L. Ni, A. Sadhanala, R. Y. S. Chen, C. Cho, L. Priest, J. M. Lim, H.-K. Kim, B. Monserrat, P. Kukura, A. Rao, Long-range ballistic propagation of carriers in methylammonium lead iodide perovskite thin films. *Nat. Phys.* 16, 171–176 (2019).
- D.-T. Nguyen, L. Lombez, F. Gibelli, S. Boyer-Richard, A. Le Corre, O. Durand,
  J.-F. Guillemoles, Quantitative experimental assessment of hot carrier-enhanced solar cells at room temperature. *Nat. Energy* 3, 236–242 (2018).
- A. V. Akimov, A simple phase correction makes a big difference in nonadiabatic molecular dynamics. J. Phys. Chem. Lett. 9, 6096–6102 (2018).
- S. Grimme, J. Antony, S. Ehrlich, H. Krieg, A consistent and accurate ab initio parametrization of density functional dispersion correction (DFT-D) for the 94 elements H-Pu. J. Chem. Phys. 132, 154104 (2010).
- P. Umari, E. Mosconi, F. De Angelis, Relativistic GW calculations on CH<sub>3</sub>NH<sub>3</sub>PbI<sub>3</sub> and CH<sub>3</sub>NH<sub>3</sub>SnI<sub>3</sub> perovskites for solar cell applications. Sci. Rep. 4, 4467 (2014).
- R. Long, J. Liu, O. V. Prezhdo, Unravelling the effects of grain boundary and chemical doping on electron-hole recombination in CH<sub>3</sub>NH<sub>3</sub>Pbl<sub>3</sub> perovskite by time-domain atomistic simulation. J. Am. Chem. Soc. 138, 3884–3890 (2016).

#### Acknowledgments

**Funding:** The work at Purdue (T.W., L.J., J.M.S., S.D., T.Z., and. L.H.) is supported by the U.S. Department of Energy, Office of Basic Energy Sciences through award DE-SC0016356. W.C. and O.P. acknowledge support of the U.S. National Science Foundation, grant no. CHE-1900510. **Author contributions:** L.H. and T.W. designed the experiments. T.W., L.J., J.M.S., S.D., and T.Z. carried out the optical measurements. T.W., L.J., and L.H. analyzed the optical measurements. J.H., J.-P.C.-B., and B.L. contributed to sample growth and performed x-ray structural characterizations. W.C. and O.P. carried out and analyzed the DFT calculations. T.W. and L.H. wrote the manuscript with input from all authors. **Competing interests:** The authors declare that they have no competing interests. **Data and materials availability:** All data needed to evaluate the conclusions in the paper are present in the paper and/or the Supplementary Materials. Additional data related to this paper may be requested from the authors.

Submitted 1 February 2020 Accepted 11 September 2020 Published 23 October 2020 10.1126/sciady.abb1336

Citation: T. Wang, L. Jin, J. Hidalgo, W. Chu, J. M. Snaider, S. Deng, T. Zhu, B. Lai, O. Prezhdo, J.-P. Correa-Baena, L. Huang, Protecting hot carriers by tuning hybrid perovskite structures with alkali cations. *Sci. Adv.* **6**, eabb1336 (2020).



# Protecting hot carriers by tuning hybrid perovskite structures with alkali cations

Ti Wang, Linrui Jin, Juanita Hidalgo, Weibin Chu, Jordan M. Snaider, Shibin Deng, Tong Zhu, Barry Lai, Oleg Prezhdo, Juan-Pablo Correa-Baena and Libai Huang

Sci Adv **6** (43), eabb1336. DOI: 10.1126/sciadv.abb1336

ARTICLE TOOLS http://advances.sciencemag.org/content/6/43/eabb1336

SUPPLEMENTARY MATERIALS http://advances.sciencemag.org/content/suppl/2020/10/19/6.43.eabb1336.DC1

This article cites 44 articles, 9 of which you can access for free http://advances.sciencemag.org/content/6/43/eabb1336#BIBL REFERENCES

PERMISSIONS http://www.sciencemag.org/help/reprints-and-permissions

Use of this article is subject to the Terms of Service